

Time-resolved investigation of a high-repetition-rate gas-jet target for high-harmonic generation


Balázs Nagyillés^{1,2,*}, Zsolt Diveki¹, Arjun Nayak¹, Mathieu Dumergue^{1,3}, Balázs Major^{1,4}, Katalin Varjú^{1,4} and Subhendu Kahaly^{1,2,†}

¹ELI ALPS, ELI-HU Non-Profit Ltd., Wolfgang Sandner utca 3., Szeged 6728, Hungary

²Institute of Physics, University of Szeged, Dóm tér 9, Szeged H-6720, Hungary

³LULI-CNRS, CEA, Sorbonne Université, Ecole Polytechnique, Institut Polytechnique de Paris, Paris, France

⁴Department of Optics and Quantum Electronics, University of Szeged, Dóm tér 9, Szeged H-6720, Hungary

 (Received 14 June 2023; revised 13 September 2023; accepted 12 October 2023; published 22 November 2023)

High-repetition-rate gas targets constitute an essential component in intense laser matter interaction studies. The technology becomes challenging as the repetition rate approaches the kilohertz regime. In this regime, cantilever-based gas valves are employed, which can open and close in tens of microseconds, resulting in a unique kind of gas characteristics in both the spatial and temporal domain. Here we characterize piezo cantilever-based kilohertz pulsed gas valves in the low density regime, where it provides sufficient peak gas density for high-harmonic generation while releasing a significantly smaller amount of gas reducing the vacuum load within the interaction chamber, suitable for high-vacuum applications. In order to obtain reliable information of the gas density in the target jet, space-time resolved characterization is performed. The gas-jet system is validated by conducting interferometric gas density estimations and high-harmonic generation measurements at the Extreme Light Infrastructure Attosecond Light Pulse Source facility. Our results demonstrate that while employing such targets for optimal high-harmonic generation, the high intensity interaction should be confined to a suitable time window, after the cantilever opening. The measured gas density evolution correlates well with the integrated high-harmonic flux and state-of-the-art three-dimensional simulation results, establishing the importance of such metrology.

DOI: [10.1103/PhysRevApplied.20.054048](https://doi.org/10.1103/PhysRevApplied.20.054048)

I. INTRODUCTION

Investigations in ultrashort laser-plasma science in the strong field regime are generically based on the interaction of an appropriately focused laser driver onto reflective (overdense) or transparent (underdense) targets. The interaction conditions need to be reproduced, and hence, the target needs to be replenished, at the repetition rate of the laser. Recent advances in few cycle, high peak power high-repetition-rate (≥ 1 kHz) lasers [1–4] has expedited the development and characterization of targets that are able to sustain interactions at such a challenging repetition rate in a reproducible and stable manner. For all transmission-based experiments in this domain, the use of gas targets is

widespread because they can provide a dense, stable, and reproducible medium for laser matter interaction studies.

The application space is ever expanding with recent demonstrations of the laser wake field acceleration of electrons [5,6] and high-harmonic-based *attosecond* pulse generation [7–10], both operating at a high repetition rate. In both cases a continuous gas cell has been used for the interaction and the accessible gas density space is limited due to the residual gas load within the vacuum chamber. One straightforward way to overcome this is to use a high-repetition-rate gas-jet target with appropriate nozzle geometry. Pulse valves working up to a very high pressure and gas density has been demonstrated [11], albeit operating at a low frequency. Nonetheless, the available repetition rate for pulsed valves currently allows one to reach up to approximately 5 kHz [12–15]. The importance of careful metrology of gas jets emanating from such valves with respect to their appropriate application space cannot be overemphasized. Such systems are important for the *attoscience* community and beyond. For example, coupled with the emergence of ≥ 1 kHz intense lasers [1–4] such a high-repetition-rate gas-jet target can enable the extension of the recent demonstrations like multimillijoule terahertz

*balazs.nagyilles@eli-alps.hu

†subhendu.kahaly@eli-alps.hu

Published by the American Physical Society under the terms of the [Creative Commons Attribution 4.0 International](https://creativecommons.org/licenses/by/4.0/) license. Further distribution of this work must maintain attribution to the author(s) and the published article's title, journal citation, and DOI.

[16] and/or relativistic single-cycle mid-infrared (mid-IR) pulses [17,18] to the high average power regime, opening up wide ranging applications. The capability of solenoid type Even-Lavie valves operating at less than 2 kHz repetition rate has been demonstrated in the domain of high harmonic spectroscopy of molecules [19,20] and transient absorption spectroscopy [21]. Here we undertake the space and time-resolved investigation of the gas density profile of a piezo cantilever-based high-repetition-rate gas jet from the perspective of optimizing the high-harmonic generation (HHG).

HHG is a nonlinear process where the strong fundamental laser field gets coherently up-converted to a comb of higher frequency radiation [22]. This frequency conversion happens in a gas target for most of the cases, when the atomic or molecular system of the gas is driven in the strong field regime [23,24]. The conversion efficiency is inherently defined by the HHG process that is dependent on the characteristics of the generating laser pulse and the gas medium. One of the parameters to optimize the high-harmonic radiation is the pressure of the gas target, since the number of particles determine the number of emitters and absorbers in the HHG and define the phase mismatch. There is a fine balance between increasing the number of emitters and absorbing the generated harmonics [25,26] for a given set of laser parameters. Thus, it is evident that proper gas target characterization is essential for optimization of the HHG process.

In this paper we perform interferometric characterization of the space-time resolved gas density profile and study the HHG from a cantilever-based high-repetition-rate piezo gas-jet system. Our investigation reveals a clear correlation of the HHG yield and dynamics of the gas density evolution. We further corroborate our observation with three-dimensional (3D) strong field simulations that incorporate microscopic HHG along with macroscopic propagation effects emulating the experimental conditions. Our results show that the gas density profile resulting from such a valve is intricately linked to the dynamics of the cantilever piezo. The remarkable correlation of the HHG signal with the gas density dynamics allows us to achieve a stable and optimum harmonic signal through carefully setting the timing of the valve opening with respect to the pulse arrival. This also establishes the importance of such space-time resolved characterization for each such high-repetition-rate piezo cantilever-based valve for any given application under consideration. This becomes crucial in systems like the SYLOS compact beamline at the extreme light infrastructure attosecond light pulse source (ELI-ALPS) [27,28] where several high-repetition-rate pulsed gas jets can be placed in sequence [29], in order to improve extreme-ultraviolet (XUV) beam energy, by optimizing the phase matching conditions for applications in nonlinear XUV physics [30–32], and also potentially in the case of newly proposed compact setups [33].

II. EXPERIMENTS

The required behavior of a gas jet in HHG is its short opening time, while creating a high density jet at its orifice at high repetition rate. It is crucial to reliably synchronize the timing of the nozzle opening of the gas jet and the arrival of the generating laser pulse, in order to get the best harmonic yield. The experiments have been conducted at two separate locations. We developed a standalone test station to characterize the gas density inside the jet under different timing of the trigger, valve opening time, and backing pressure. We used the outcome to compare it to the harmonic yield obtained from the experiments conducted at the SYLOS compact beamline [27,28] at ELI-ALPS.

A. Gas-jet characterization by interferometry

The density profiling of gas targets has been carried out with several different methods (see Ref. [34] and references therein) for both static [34] and pulsed jets [35–38]. Here we undertake space-time resolved interferometry to access the gas atomic density distribution. The experimental layout is based on an Mach-Zehnder interferometer; see Fig. 1(a). An expanded He-Ne laser is used to enter the interferometer after being split in two arms. The interaction arm passes through a gas jet to introduce some phase shift in the optical path of the laser beam with respect to the reference arm. Both arms are in vacuum. The gas target transverse plane [represented by $I_1(y, z)$ in Fig. 1(a)] is imaged onto a CMOS sensor (a commercial Basler acA1440-73gm camera), where the recombined beams form the interference pattern [$I_{12}(y, z)$ in Fig. 1(b)]. The following vital points have been taken into account when characterizing the gas jets.

(a) To keep the signal-to-noise ratio high (especially at low gas-jet densities) an ATH 500M turbomolecular pump was providing the low ambient pressure in the chamber, 10^{-5} – 10^{-6} mbar. Additionally, the whole part of the interferometer, which is not in vacuum, had to be covered to protect the beam paths from air fluctuations and the assembly was placed on a stable optical table. These precautions reduced the residual gas load, minimized parasitic vibrations, and reduced refractive-index fluctuations in the interferometer, allowing the intrinsic noise of the setup to be limited to gas density levels as low as about $3 \times 10^{17} \text{ cm}^{-3}$, estimated from the analysis of reference images of the interference pattern, without activating the valve.

(b) The experimental target gas is argon that has a high refractive index of 1.00028 at wavelength $\lambda = 633 \text{ nm}$ (for example, significantly higher compared with helium 1.000034 at the same wavelength) allowing for more sensitivity in terms of measuring phase difference, in spite

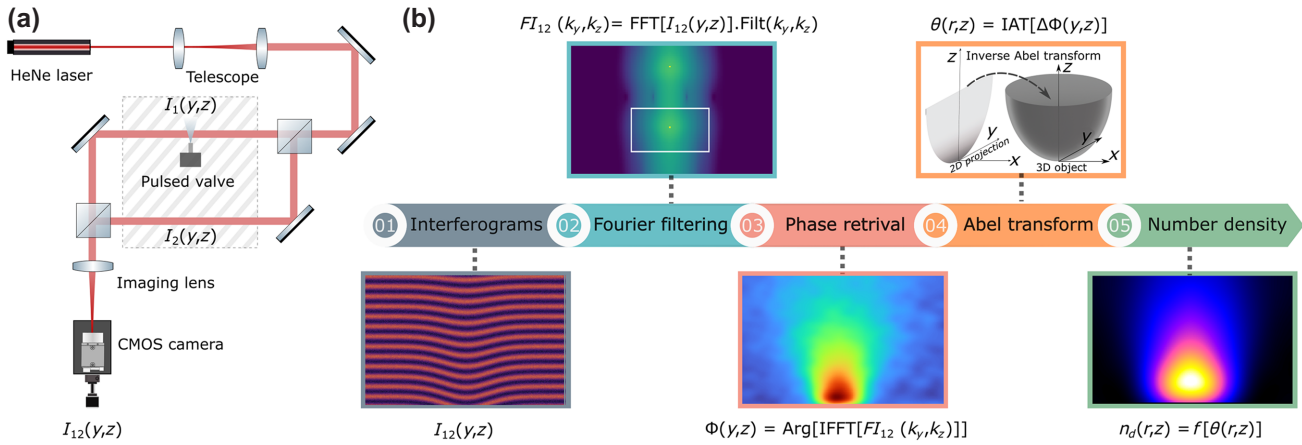


FIG. 1. Interferometric setup for gas density profile measurements for (a) the gas jet based on a high frequency cantilever valve and data analysis flow, and (b) for number density extraction from the measured interferograms. (a) Schematic layout of the pulsed jet density characterisation setup. A Mach-Zehnder setup is used to extract the projection interferograms $I_{12}(y, z)$. The camera images the gas-jet plane and $I_{12}(y, z)$ is formed by interference of the spatial field distribution in the gas-jet plane (interaction arm indicated by $I_1(y, z)$) and an equivalent plane in the other arm (reference arm indicated by $I_2(y, z)$). (b) Steps of the Abel transform based gas density extraction. (01) Acquisition of interference pattern from the interferometer. (02) A 2D Fourier transform of the interference pattern and filtering the zone of interest in the Fourier space with an appropriate mask. (03) The accumulated phase $\phi(y, z)$ due to the optical path difference between the two arms is extracted from the inverse Fourier transform of $FI_{12}(k_y, k_z)$. For each gas density extraction, $\phi(y, z)$ is retrieved with gas ($\phi_g(y, z)$) and without gas ($\phi_0(y, z)$). The difference between these two terms give the contribution of phase due to the presence of gas, $\Delta\phi(y, z) = \phi_g(y, z) - \phi_0(y, z)$. In (04) the inverse Abel transform (IAT) is utilized on $\Delta\phi(y, z)$ (on the retrieved path difference), to obtain the radial and vertical phase variation $\theta(r, z)$ in the laser beam due to the gas jet. Finally, in (05) this phase variation is converted to the refractive index, $n(r, z) = (\lambda/2\pi)\theta(r, z) + 1$, and the number density $n_d(r, z)$ is extracted from the functional dependence of n on n_d . The images in (b) represent the typical data at each step of the analysis protocol.

of the submillimetric width of the gas jet, even in the sub- 10^{18} cm^{-3} density regime.

(c) The gas refractive-index *ansatz* is valid, when the characterization is not corrupted due to molecular jet formation with large clusters. Within the parameter range relevant to us, the empirical Hagena parameter $\Gamma^* \ll 100$ is significantly less than the limit $\Gamma^* \sim 10^3$ required for cluster formation [39–41].

For the tests, we used an Amsterdam piezo valve ACPV3 model, a cantilever piezo with a 500- μm nozzle size (Appendix A). Cantilever piezos can deliver large displacements up to hundreds of micrometers to 1 mm, while working at high repetition rates, up to 5 kHz. The difference of the cantilever piezos to disk-shaped piezos is that by adjusting the free length of the cantilever one can adjust the displacement of the cantilever [12]. For example, by decreasing the length, the displacement drops rapidly, while its resonant frequency increases. Cantilever resonance can introduce observable effects in gas density measurement. Since the cantilever will bounce back and forth while opening and closing the pulsed valve, it can introduce pressure and, hence, number density fluctuation in the released gas within one such cycle of operation.

The synchronization between the camera and the jet is realized with a delay generator. The time resolution of the

measurement—which is determined by the shortest possible exposure time of the CMOS sensor—is 1 μs . For each measurement, two images are recorded, one with the nozzle opened and one with the nozzle closed serving as a reference measurement without any gas present in any arms—this is realized by running the camera at twice the repetition rate of the gas source. For resolving the temporal evolution of the gas density while opening the valve, the camera trigger was delayed compared with the trigger signal of the jet. The setup can record images at up to 100 Hz, but in order to get a background free image one has to wait until the turbomolecular pump can reduce the pressure in the chamber to the base— 10^{-5} – 10^{-6} mbar level, resulting in a few hertz operation (further details can be found in Appendix A).

As depicted in the flow chart in Fig. 1(b), the two-dimensional (2D) phase shift $\phi(y, z)$ is extracted from the interferogram using the 2D Fourier transformation algorithm described in Ref. [42]. One can see from a typical unwrapped phase map presented in Fig. 1(b) (step 3) that in the plane perpendicular to the propagation axis x , the jet rapidly spreads out as the distance from the nozzle tip increases (vertical z direction). The extra contribution to the phase shift introduced in the probe beam propagating along x by the argon gas density profile is $\Delta\phi(y, z) = \int (2\pi/\lambda)\Delta n(x, y, z)dx$, where $\Delta n(x, y, z) = n(x, y, z) - 1$

is the shift in index of refraction due to the presence of the gas and $n(x, y, z)$ is the refractive index of the argon jet. As explained in the caption of Fig. 1, $\Delta\phi(y, z)$ is calculated from two projection interferograms: one with the gas jet on and the other without any gas in the interaction arm.

The measured phase map $\Delta\phi(y, z)$ is a 2D projection of the 3D distribution of the phase difference $\Delta\phi(r, z)$ introduced by the gas jet (r is the radial distance from the center of the gas-jet axis z). Since one can assume that the jet has a cylindrical symmetry, it is possible to transform the projection $\Delta\phi(y, z)$ to a radial distribution $\theta(r, z) = \Delta\phi(r, z)$ using the inverse Abel transform (IAT) [43],

$$\begin{aligned} \theta(r, z) &= \text{IAT}[\Delta\phi(y, z)] \\ &= -\frac{1}{\pi} \int_r^\infty \frac{d\Delta\phi(y, z)}{dy} \frac{1}{\sqrt{y^2 - r^2}} dy, \end{aligned} \quad (1)$$

where r is the radial distance from the center of the nozzle, z is the vertical distance from the tip of the nozzle, and transverse coordinate y is the coordinate perpendicular to x and z . This is indicated in step 4 of Fig. 1(b).

We numerically carry out the IAT in PYTHON using the well-developed basis set expansion (BASEX) [44] method in the package PyAbel [45]. The refractive index can be expressed with the radial distribution using $\Delta n(r, z) = n(r, z) - 1 = (\lambda/2\pi)\theta(r, z)$, where λ is the wavelength of the laser. The refractive index is connected to the number density. This can be found through the series of a few steps. The molar reflectivity (A) relates the optical properties of the substance with the thermodynamic properties. From the Lorenz–Lorentz expression that is dependent on the temperature (T) through the molar mass (M), $A = [(n^2 - 1)/(n^2 + 2)](M/\rho)$, where n is the refractive index of the atomic gas and ρ is the gas density [37]. The molar mass can be given by $M = RT\rho/p$, where R is the universal gas constant and p is pressure. Using the relation between polarizability ($\alpha_e = 1.664 \text{ \AA}^3$ for argon) and molar reflectivity, $A = (4/3)N_A\alpha_e\pi$ and ideal gas law as $pV = NRT$, the number density $n_{md} = N/V$ in the units of particles/cm³ can be written as

$$n_d = \frac{n_{md}}{N_A} = \frac{3(n^2 - 1)}{4(n^2 + 2)} \frac{1}{N_A^2 \alpha_e \pi}. \quad (2)$$

This is the last step presented in Fig. 1(b).

B. High-harmonic generation in the beamline

The gas density dynamics during the opening and closing of the cantilever is crosschecked on the SYLOS compact beamline [27,28]. The main goal of this beamline is to achieve high energy isolated *attosecond* pulses as well as *attosecond* pulse trains in the sub 150 eV regime at high repetition rate, in order to perform XUV-pump XUV-probe

nonlinear experiments [31,32]. To achieve this goal, it uses long laser focusing (10 m) and up to four high pressure gas jets to generate XUV radiation. The generated XUV beam is separated from the driver IR by a 200 nm thick Al filter and the XUV signal is detected with a calibrated XUV photodiode. The incoming beam size is around 6 cm that is reduced with an iris to 3 cm in order to maximize the XUV yield—resulting in around 12 mJ in the interaction region. These conditions enable the generation of around 30 nJ XUV pulses, from argon gas, after XUV filter.

The driving laser for this experiment was the SYLOS experiment alignment laser [46] that operates at 10 Hz and delivers 34 mJ pulse energy with 11 fs pulse duration at 825 nm central wavelength. When optimizing the XUV energy, it is crucial to get the timing of the valve opening and the opening duration correct for the individual gas jets, in order to maximize the gas density in each interaction region. By keeping the valve opening time constant and changing the delay between the laser trigger and the opening of the valve one can study the impact of the dynamics of the valve opening on the integrated yield of the generated XUV. In an ideal case there is a rise in the gas density as the valve opens, so the XUV yield grows, then it reaches a maximum, when the valve opens the most. The gas density corresponding to the maximum valve opening should stay fairly constant during the opening time of the valve, then it should slowly drop to zero with the closing valve. This is the typical behavior at the disk-shaped piezo valve. We show that the gas density does not stay constant during the opening time of the cantilever piezo valve, which introduces an extra factor to optimize during the high-harmonic generation.

III. RESULTS

A. Experimental observations

In Fig. 2(a) we present the retrieved gas atomic number density distribution along the radial (please note that the radial r , x , and y distributions are the same due to the cylindrical symmetry of the gas flow) and the vertical direction, achieved by applying the protocol presented in the previous section. The presented density map is achieved at one specific delay after opening of the gas valve. Because of the shape of the nozzle, the expanding gas jet is rather confined into a cylinder along the vertical direction with a diameter of 500 μm (which is the opening size of the nozzle) and not expanding much in the radial direction. As expected, the maximum value of the number density distribution is close to the exit of the valve and its value is around 1.2×10^{19} particles/cm³. The central z lineout $n_d(r = 0, z)$ presented in Fig. 2(b) shows the exponential decay of the number density distribution as the distance from the nozzle increases in the vertical direction, a typical feature of such nozzle geometry [11,35]. In Fig. 2(c)

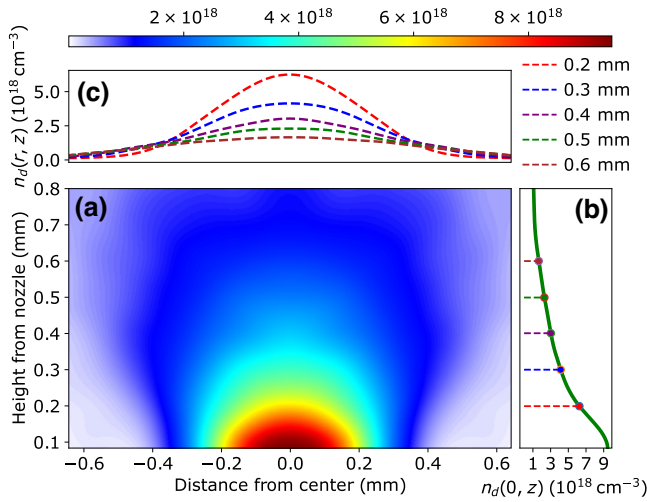


FIG. 2. (a) The distribution of the number density of the gas along the radial and the vertical direction. The corresponding colorbar is located at the top of the figure and is expressed in atoms/cc. (b) The vertical decay of the gas number density from the center of the nozzle (radial position 0.0 mm) as one moves away from the nozzle (green line). The circles with their horizontal dashed lines show the vertical position of the outlines of the (c) radial gas density distribution. The actual vertical distances of these lineouts are shown in the top right corner.

we plot the radial lineouts of $n_d(r, z)$ for the five different z values marked in Fig. 2(b).

In all the measurements the opening window of the valve is set to 400 μs . In Fig. 3(a) we present five different snapshots of the dynamic evolution of the gas number density distribution in space, within the opening window of the gas valve. As discussed before, the gas density is exponentially dropping as a function of height from the nozzle exit. Therefore, in order to access the higher density region for the HHG experiments, for the given focusing configuration, one has to shoot as close to the exit of the nozzle as possible, without damaging the nozzle. Because of technical constrains, for our conditions, in the HHG experiments we kept the center of the intense focused beam around 400 μm above the exit. The black dashed horizontal lines on the colormaps in Fig. 3(a) represent the laser propagation axis ($z = 400 \mu\text{m}$) for HHG experiments. The red solid circles in Fig. 3(a) indicate the position of maximum atomic gas density along the laser propagation axis. These colormaps show that during the opening time of the valve the laser focus experiences large variations in the gas distribution. In order to closely follow the temporal evolution we obtain a large number of 2D spatial gas number density snapshots as a function of delay within the opening window of the valve. In Fig. 3(b) we plot the maximum number density seen by the center of the laser focal spot as a function of this delay. The vertical red lines in Fig. 3(b) indicate the temporal delay where the 2D number density

snapshots [presented in Fig. 3(a)] were taken, while the red circles and the black curve correspond to the maximum gas number density in the focal spot.

In an ideal case, during the scan of the opening window one would see the rise then the drop of the number of particles in the interaction region, while the maximum would show the right delay setting for optimal harmonic yield. However, in our case, in Fig. 3(b) we clearly identify several maxima as a function of the delay. Time-dependent injection of the gas jet within the pulsed valve aperture time and a consequent gas density depletion has been observed by other research groups as well [35,36,38]. One can observe two important features on the graph in Fig. 3(b): on one hand, the opening and closing of the valve is not sudden, but takes several tens of microseconds; on the other hand, during the opening window, the signal oscillates. The first minimum is a drop of approximately 40% in the number density, while the following drops are less intense. However, the maxima reaches roughly the same level in each case. The observed facts are a clear sign of a damped oscillation of the cantilever piezo [12] that is well known from vibrations of cantilever beams [47]. The frequency of this oscillation is roughly 7.6 kHz, determined by physical parameters of the piezo and not influenced by the driving frequency [12]. The results show that the dynamics of the cantilever when using it as a valve introduces variations in the gas-jet density profile, emphasizing the importance of such metrology in any experiment that is sensitive to the gas atomic number density. In addition, since the gas expansion from such a valve is nontrivial, the knowledge of the exact distribution of gas density could improve the understanding and modelling of the HHG process, while correlating with experimental observations.

Figure 3(c) presents the normalized high-harmonic yield (red rectangles) as a function of the delay of the arrival time of the interacting intense focused laser pulse with respect to the opening time [marked as zero delay that signifies a measurable number density above the detection threshold in Fig. 3(b)] of the valve. The relative high-harmonic yield is experimentally measured with a thin film coated photodiode (Optodiode-AXUV100AL). The HHG yield data presented in Fig. 3(c) is normalized with respect to the maximum measured yield. The red vertical lines correspond to the delay times presented in Fig. 3(a). Multiple red rectangles at the same delay time [when available are presented in Fig. 3(c)] represent typical fluctuations in the measured yield. The measured HHG yield data in Fig. 3(c) follows remarkably well the number density variations presented in Fig. 3(b).

For the HHG interaction, we note the following points.

(a) The laser-pulse duration (approximately 11 fs FWHM of the pulse intensity envelop) is negligible on

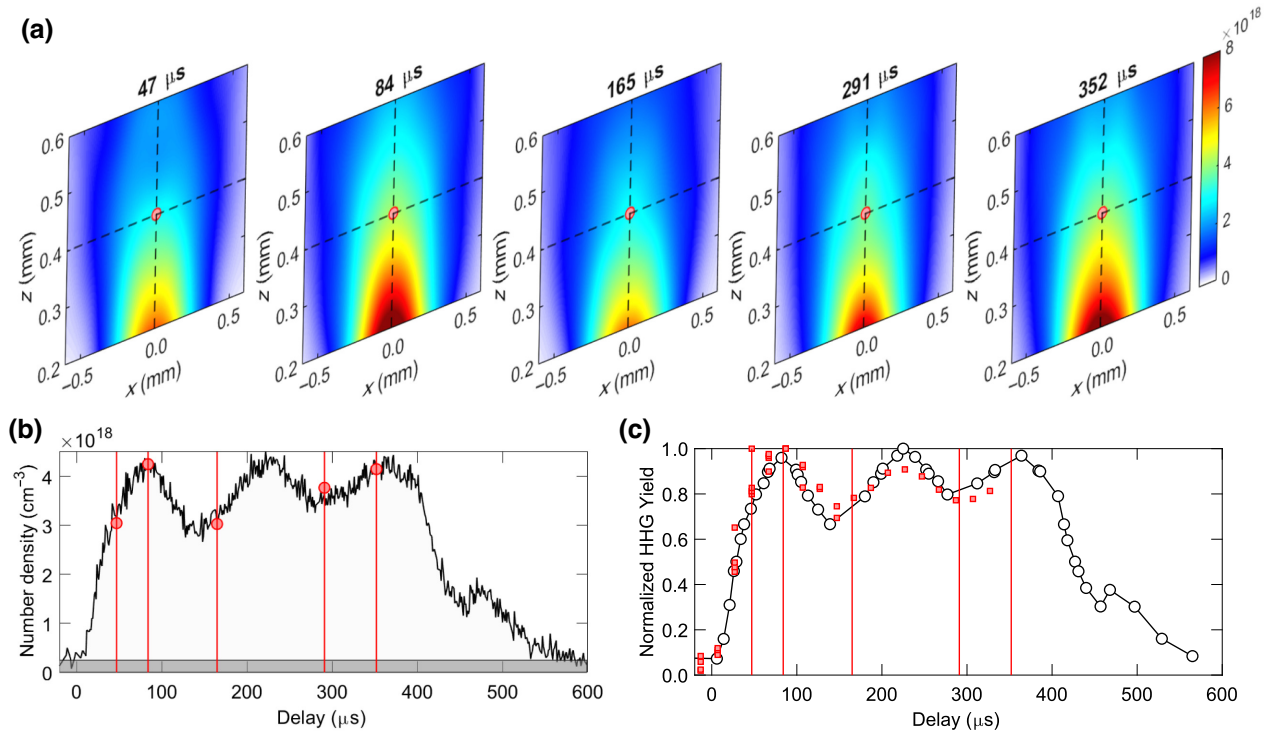


FIG. 3. (a) The spatial distribution of measured 2D gas atomic density profiles $n_a(x, z, t)$ [$= n_a(y, z, t)$] as a function of delay from valve opening. The black dashed vertical line along y defines the gas-jet symmetry axis and the dashed horizontal line x is along the laser propagation direction during strong field interaction. The colorbar represents atomic density in atoms/cc. The red shaded circle at the center of each gas density slice indicates the reference point where the interaction is centered. (b) Gas atomic density at the same point as a function of delay time (the black curve). The dynamics of the high-repetition-rate cantilever valve opening and closing leads to a characteristic variation of gas density as a function of delay. The vertical red lines correspond to the delays at which the spatial profile is presented in (a). The corresponding data points are indicated in red dashed circles in the figure. The gray shaded horizontal region indicates the detection threshold by our interferometric technique, below which data becomes noisy. (c) The red dashed rectangles depict the variation in high-harmonic yield (normalized to the maximum) at different time delays. The black hollow circles demarcate the same, but this time calculated from simulations that mimic experimental gas density conditions. The variation in high-harmonic yield in (c) shows striking resemblance to the gas density curve presented in (b).

the timescale of gas density evolution. This implies that the interacting pulse sees a frozen gas density distribution in the transverse plane. This ensures that the microscopic emitter distribution across the focal spot, within the pulse duration during HHG are not evolving.

(b) The transit time of the intense laser pulse through the gas-jet target (typically < 10 ps in our case) is also negligible compared with the timescale of gas dynamics. This ensures that the measured temporal snapshots of the spatial distribution of gas number density does not change during pulse propagation and, thus, can be utilized for macroscopic phase matching considerations in HHG.

(c) Since the confocal parameter (approximately 49 cm) is significantly larger than the medium length (approximately 1 mm) under our experimental configuration, we are not limited by longitudinal variation of intensity and the contribution of Gouy phase, associated with the spatial focusing of the fundamental laser pulse, to phase matching is unimportant.

(d) The gradient in the number density [presented in Fig. 2(b)], across the focal spot diameter of approximately 300 μm can result in subtle effects like influencing the phase matching condition for the HHG. This can lead, for example, to distortions in the XUV wavefront impacting the focusability of the XUV beam [48,49], which is beyond the scope of the present paper.

The experimental results demonstrate that in the case of HHG it is essential to know the exact number density of the gas medium in a space-time resolved manner. In addition, in order to optimize the harmonic yield one has to synchronize the arrival of the generating laser pulse with the opening time of the valve and introduce an appropriate relative time delay, depending on spatiotemporal characteristics of the gas jet under utilization.

At this point, we would like to emphasize that the monotonic nature of the HHG yield as a function of measured gas-jet atomic density, as observed experimentally and presented in Fig. 3(c), is not the case in general.

In case of coherent light emission—like HHG—the generated photon flux scales quadratically with the number of emitters under ideal conditions [50]. The resemblance between the jet density [Fig. 3(b)] and the harmonic yield [Fig. 3(c)] highlights the importance of phase matching, as it manifests under our specific experimental conditions. A close investigation of the correlation between the number density data in Fig. 3(b) and the measurements in Fig. 3(c) reveal that within our interaction regime the HHG yield is almost proportional to the gas pressure. Phase matching is a complex dynamical [51,52] process and the relation between gas atomic number density and HHG yield is not straightforward in the short pulse regime. In order to investigate further we undertake numerical simulations in the following.

B. Numerical validation using 3D simulation

Direct measurement of the gas number density distribution in the HHG interaction region is crucial not just from the optimization of the high-harmonic source. Such metrology also enables one to feed experimental measurements into state-of-the-art simulation tools that are often utilized to investigate the strong field interaction further. In this case the numerical simulations can be performed in a virtual experimental setup with initial parameters mimicking the real experimental conditions. This is important, if one needs to reconcile experimental observations with theoretical results and interpret the relevant physics in a correct manner.

In our case, we undertake such an effort and use state-of-the-art simulations where the gas-jet metrology data are fed as input to simulate the harmonic yield. We note here that the macroscopic effects such as plasma generation, absorption, and refraction during propagation play a significant part in the phase matching process and, hence, cannot be neglected for calculation of the HHG yield. In order to investigate the experimental results further, we performed a series of macroscopic simulations using a 3D nonadiabatic model, described in detail elsewhere [53–55].

As a short summary, the simulation is performed in three self-consistent computational steps. Firstly, to analyze the propagation of the linearly polarized electric field of the fundamental laser pulse $E(\mathbf{r}_L, t)$ in the generation volume, the nonlinear wave equation of the form

$$\nabla^2 E(\mathbf{r}_L, t) - \frac{1}{c^2} \frac{\partial^2 E(\mathbf{r}_L, t)}{\partial t^2} = \frac{\omega_0^2}{c^2} (1 - n_{\text{eff}}^2(\mathbf{r}_L, t)) E(\mathbf{r}_L, t), \quad (3)$$

is solved [53]. In the previous equation c is the speed of light in vacuum, ω_0 is the central angular frequency of the laser field, and the suffix L in \mathbf{r}_L indicates that this vector represents the coordinate in the frame with respect to the laser axis (in contrast to the r scalar coordinate described previously around the gas-jet symmetry

axis). The effective refractive index $n_{\text{eff}}(\mathbf{r}_L, t)$ of the excited medium—depending on both space and time—can be obtained by $n_{\text{eff}}(\mathbf{r}_L, t) = n + \bar{n}_2 I(\mathbf{r}_L, t) - (\omega_p^2(\mathbf{r}_L, t)/2\omega_0^2)$ [56], where $I(\mathbf{r}_L, t) = \frac{1}{2} \epsilon_0 c |\tilde{E}(\mathbf{r}_L, t)|^2$ is the intensity envelope of the laser field (note that in this expression the complex electric field $\tilde{E}(\mathbf{r}_L, t)$ is present [57]) and $\omega_p(\mathbf{r}_L, t) = [n_e(\mathbf{r}_L, t) e^2 / (m \epsilon_0)]^{1/2}$ is the plasma frequency. The plasma frequency is well known to be a function of the electron number density $n_e(\mathbf{r}_L, t)$, and its expression also contains the electron charge e , the effective electron mass m , and the vacuum permittivity ϵ_0 . Dispersion and absorption, along with the Kerr effect, are thus incorporated via the linear (n) and nonlinear (\bar{n}_2) part of the refractive index. Absorption losses due to ionization [58] are also included, while plasma dispersion is estimated based on ionization values in the last term of $n_{\text{eff}}(\mathbf{r}_L, t)$. The model assumes cylindrical symmetry about the laser propagation direction z_L ($\mathbf{r}_L \rightarrow r_L, z_L$) and uses paraxial approximation [56]. Applying a moving frame translating at the speed of light, and by eliminating the time derivative using Fourier transform \mathcal{F} , Eq. (3) reduces to the explicit form

$$\left(\frac{\partial^2}{\partial r_L^2} + \frac{1}{r_L} \frac{\partial}{\partial r_L} \right) E(r_L, z_L, \omega) - \frac{2i\omega}{c} \frac{\partial E(r_L, z_L, \omega)}{\partial z_L} = \frac{\omega^2}{c^2} \mathcal{F}[(1 - n_{\text{eff}}^2(r_L, z_L, t)) E(r_L, z_L, t)]. \quad (4)$$

Equation (4) is solved using the Crank–Nicolson method in an iterative algorithm [56]. The ABCD–Hankel transform is used to define the laser field distribution in the input plane of the medium [59,60].

In step two we calculate the single-atom response (dipole moment $D(t)$) based on the laser-pulse temporal shapes available on the complete (r_L, z_L) grid, by evaluating the Lewenstein integral [23,61]. The macroscopic nonlinear response $P_{\text{nl}}(t)$ is then calculated by taking the depletion of the ground state into account [61,62] using $P_{\text{nl}}(t) = n_a D(t) \exp\left[-\int_{-\infty}^t w(t') dt'\right]$, where $w(t)$ is the ionization rate obtained from tabulated values calculated using the hybrid antisymmetrized coupled channels approach [63], showing a good agreement with the Ammosov–Delone–Krainov model [64], and n_a is the atomic number density within the specific grid point (r_L, z_L) [56,65].

In the third step we calculate the propagation of the generated harmonic field $E_h(\mathbf{r}_L, t)$ using the wave equation

$$\nabla^2 E_h(\mathbf{r}_L, t) - \frac{1}{c^2} \frac{\partial^2 E_h(\mathbf{r}_L, t)}{\partial t^2} = \mu_0 \frac{d^2 P_{\text{nl}}(t)}{dt^2}, \quad (5)$$

with μ_0 being the vacuum permeability. Equation (5) is solved in a manner similar to Eq. (3), but without an iterative scheme (since the source term is known).

The amplitude decrease and phase shift of the harmonic field—caused by absorption and dispersion, respectively—are incorporated at each step when solving Eq. (5) by taking into account the effect of the complex refractive index on wave propagation. The real and imaginary parts of the refractive index in the XUV regime are from tabulated values of atomic scattering factors [66].

Figure 3(c) presents the simulated harmonic yield (black hollow circles) as a function of the delay from the opening of the valve. The gas-jet pressure for the simulation is calculated from the number density variation in Fig. 3(b). Both the HHG measurements and simulations show a remarkable resemblance to the jet density variation measured with the interferometric technique. The measured HHG spectrum in our conditions also matches well with the simulated XUV spectrum (Appendix B). We note here that, in our simulations, the single-atom response is calculated within the strong field approximation formalism, using the Lewenstein integral [23,24,61]. In this case, the relative intensity of the HHG spectra and, hence, the relative yield is calculated appropriately, but not in absolute photon numbers. In order to calculate the absolute conversion efficiency one would need to solve the time-dependent Schrödinger equation in three dimensions for the microscopic response, coupled with Maxwell's equations to take into account the propagation effects. The computational cost of such an implementation is tremendously high, and it is far beyond the scope of the current paper. In the simulations carried out here, we focus on the relative HHG yield to compare with the experiments and, for this purpose, this well-established computational approach suffices.

The simulation method described above assumes radial symmetry around the laser propagation axis. For the laser spatiotemporal profile, we use the measured focal spot distribution and experimental laser-pulse duration in order to mimic the real experimental conditions. For the gas-jet atomic number density profile, we use the measured gas jet number density profile along the axis of laser propagation [peak densities as shown in Fig. 3(b)]. Thus, within our numerical simulations, the influence of gas density gradient across the laser focal spot [along the symmetry axis of the gas jet as presented in Fig. 2(b)] is lumped into an average value.

The simulations also revealed that under the circumstances that describe these experiments, transient phase matching [67,68] limits efficient generation to the first half of the short laser pulse. At the same time, due to minimal reshaping of the pulsed laser beam, there are spatially homogeneous phase matching conditions in the whole interaction volume. This allows us to apply a simple model [25] to explain the variation of the observable harmonic flux in the absorbing medium. Specific details on this are included in Appendix C. The analysis confirmed that with the coherence lengths and absorption lengths involved, the

harmonic flux changes close to linearly with the change of atom number density.

IV. CONCLUSIONS

On one hand, an interferometric gas density characterization was developed for underdense gas jets produced from a high frequency (up to 5 kHz) cantilever piezo valve. On the other hand, we show that the cantilever valve has its characteristic dynamics while opening the valve resulting in the oscillation of the gas density as a function of time. Using HHG from such a gas-jet target, we observe a remarkable experimental correlation in between the gas density and HHG yield. Our results have been corroborated by sophisticated simulations that self-consistently include both microscopic HHG and macroscopic propagation effects under conditions mimicking the real experimental scenario. Our results establish the feasibility of utilizing cantilever-based high-repetition-rate gas valves for HHG, emphasizing the importance of precise timing control in order to access the proper gas density regime. This also shows that appropriate time and space resolved characterization and monitoring of such gas valves is an important aspect for its application and reproducible performance, which is easily achieved by properly managing the synchronization of the gas jet with respect to the arrival time of the laser. As demonstrated recently, a general systematic improvement of the high-harmonic yield can be achieved by choosing an optimal phase matching regime on the pressure-medium length hyperbola [69,70]. For such optimization and model validation, the metrology presented in this investigation would be an essential prerequisite. The results are also important to a diverse field of studies that can benefit from high-repetition-rate gas jets, where the signature effects of the phenomena have sensitive dependence upon the precise gas density profile such as molecular or atomic quantum path interferometry [71,72], ion spectroscopy from dilute plasma [73,74] spatiotemporal [75] and equivalently spatio-spectral [49,76] control of attosecond pulses, and in designing of gas-based extreme-ultraviolet refractive optics [48], to name a few.

ACKNOWLEDGMENTS

ELI ALPS is supported by the European Union and co-financed by the European Regional Development Fund (ERDF) (GINOP-2.3.6-15-2015-00001). This project has received funding from the European Union Framework Programme for Research and Innovation Horizon 2020 under IMPULSE grant agreement no. 871161. S.K. acknowledges Project No. 2020-1.2.4-TÉT-IPARI-2021-00018, which has been implemented with support provided by the National Research, Development and Innovation Office of Hungary, and financed under the 2020-1.2.4-TÉT-IPARI-CN funding scheme. We acknowledge KIFÜ for awarding us access to HPC resource based in Hungary.

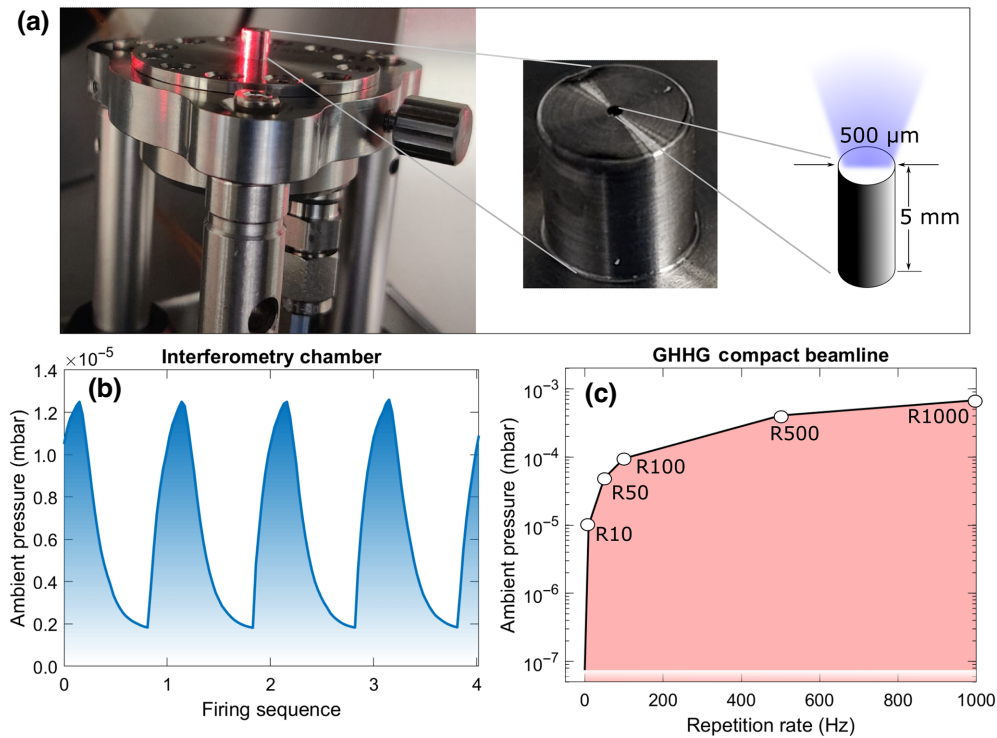


FIG. 4. (a) Nozzle geometry in the valve. The inset in the middle of the panel shows a zoomed image of the cylindrical gas outlet of ACPV3 [77] and the rightmost panel shows the inside geometry of the nozzle with a length of 5 mm and orifice diameter of 500 μm . (b) Ambient pressure variation in the interferometric chamber, where density measurements are performed, presented for the case of gas jet fires at 0.5 Hz and data acquisition from the pressure gauge is made at 17 Hz. (c) Ambient pressure level in the SYLOS GHHG compact beamline as a function of repetition rate of the gas-jet target up to 1 kHz. The white shaded region below 10^{-7} mbar level represents the base vacuum level in the beamline.

APPENDIX A: AMBIENT CHAMBER PRESSURE AND OPERATIONAL FEASIBILITY AT HIGHER REPETITION RATE

In all our experiments we use the cylindrical nozzle geometry as shown in the Fig. 4(a). For the interferometric measurements, we monitored the ambient vacuum level during the nozzle operation. Figure 4(b) shows the periodic variation of the pressure level due to the gas load introduced by the gas valve into the chamber. In this case, to capture this variation in detected pressure, we run the nozzle at approximately 0.5 Hz and acquire data from the pressure gauge at approximately 17 Hz. The pressure level fluctuates in the range of approximately 10^{-5} – 10^{-6} mbar. We did the ambient pressure measurement with increasing repetition rate of the nozzle in the SYLOS GHHG compact beamline at ELI-ALPS. The gas load data are presented in Fig. 4(c). In this case each data point represents the maximum pressure level reached under stable operation of the gas valve. In Fig. 4(c) the circles represent the measured values and “Rn” represents the data point when the repetition rate is “n” ($n = 10, 50, 100, 500, 1000$) Hz. This shows that in the beamline even at 1 kHz the ambient pressure level stays below a few times 10^{-4} mbar.

The data shows that in the case of Ar gas one can maintain a high-vacuum level for the generation chamber of the beamline, even when the valve is backed with a relatively high (3.5 bar) pressure. The data in general would depend on the pumping rate and the specific design of the vacuum chambers and, thus, can be improved further.

APPENDIX B: TYPICAL HHG SPECTRA FROM EXPERIMENT AND SIMULATION

In the main text the presented XUV photodiode measurement represents the yield within the 200 nm Al filter transmission window. Under typical experimental conditions presented in the paper, we also measured the HHG spectrum. One such representative spectrum for Ar gas is presented in Fig. 5. The HHG spectrum obtained from our numerical simulations are presented in the same plot.

We note that in our numerical simulations the single-atom calculations are performed based on the Lewenstein integral and it does not take into account properly the Cooper minimum [72], near which we see a dip in the Ar HHG spectra and it is this region where the simulated spectrum overestimates the experimental measurement. Nonetheless, for the yield, the maximum contribution is

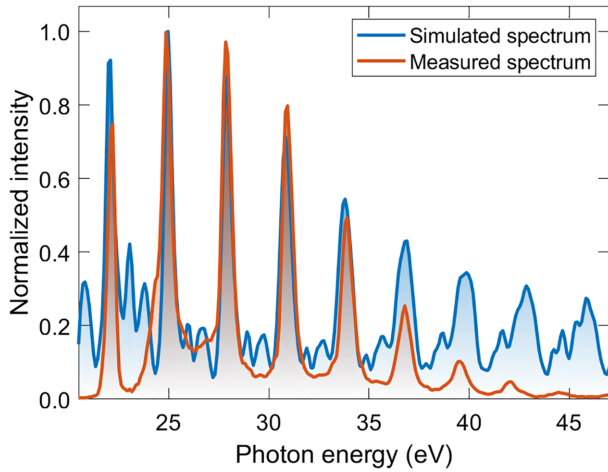


FIG. 5. Measured and simulated high-harmonic spectra in Ar gas. Both the spectra are normalized with respect to the maximum harmonic intensity around 25 eV. The spectra show that most of the HHG is occurring between 25–40 eV.

coming from the region between 25 to 40 eV as expected from the qualitative estimates in the previous section.

APPENDIX C: DISCUSSION ON THE SIMPLE MODEL REPRODUCING THE XUV FLUX DEPENDENCE WITH PRESSURE

Constant *et al.* [25] developed a simple model for optimization of high-harmonic flux S . This model leads to the formula [26]

$$S = \frac{4A^2}{\sigma^2} \frac{1}{1 + R_0^2} [1 + \exp(-2L) - 2 \cos(R_0 L) \exp(-L)], \quad (\text{C1})$$

where A is the single-atom signal strength, σ is the photoionization cross section, $L = L_{\text{med}}/(2L_{\text{abs}})$ is medium length L_{med} normalized to twice the absorption length L_{abs} , and $R_0 = 2\pi L_{\text{abs}}/L_{\text{coh}}$ is expressing the ratio of the absorption and coherence lengths (L_{coh}). Apart from medium length, all quantities in Eq. (C1) depend on the harmonic order q . The most important property of this expression [Eq. (C1)]—and what makes it easy to use it for optimization of the harmonic signal—is that the flux depends only on three parameters: the coherence length L_{coh} , the absorption length L_{abs} , and the medium length L_{med} . This way a single plot gives all the guidance necessary to optimize the high-harmonic yield (see Fig. 6, or Fig. 1 of Ref. [26]). The goals of the present section are as follows.

(a) To describe the way we use this analytical model to explain the observation in our experiments that the high harmonic flux is proportional to the medium pressure in the gas-jet target.

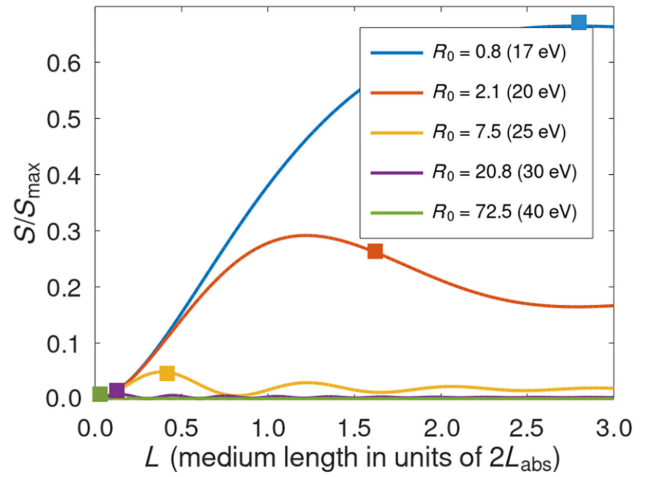


FIG. 6. The harmonic flux S normalized to the absorption-limited maximum flux $S_{\text{max}} = 4A^2/\sigma^2$ as a function of medium length $L = L_{\text{med}}/(2L_{\text{abs}})$ for different ratios of the coherence and absorption lengths, defined by $R_0 = 2\pi L_{\text{abs}}/L_{\text{coh}}$ [26] [see Eq. (C1) and related text for explanation]. The values in parentheses in the legend refer to the photon energies to which the specific curves correspond to in the experimental case described in the paper. The rectangle on each curve is the point corresponding to 2×10^{18} $1/\text{cm}^3$ atom number density; see details later in text.

(b) To detail our method to extract the L_{coh} , L_{abs} , and L_{med} parameters from experimental data and macroscopic simulations in order to apply with Eq. (C1).

Obtaining the coherence length L_{coh} is a crucial and relatively complex task, as phase matching depends on multiple factors, and through the relation [50]

$$L_{\text{coh}} = \pi/\Delta k, \quad (\text{C2})$$

coherence length also does. The total phase mismatch Δk in Eq. (C2) is usually written as the sum of four factors [50],

$$\Delta k = \Delta k_d + \Delta k_g + \Delta k_n + \Delta k_p, \quad (\text{C3})$$

representing the phase mismatch due to dipole and geometric phases, along with neutral and plasma dispersion, respectively [26,50]. Typical values of these phase mismatch terms for the current scenario are presented in Fig. 7, while calculation details are given below.

The dipole-induced phase mismatch Δk_d was calculated using Eq. (6) of Ref. [50],

$$\Delta k_d = \alpha \frac{\partial I(z)}{\partial z}, \quad (\text{C4})$$

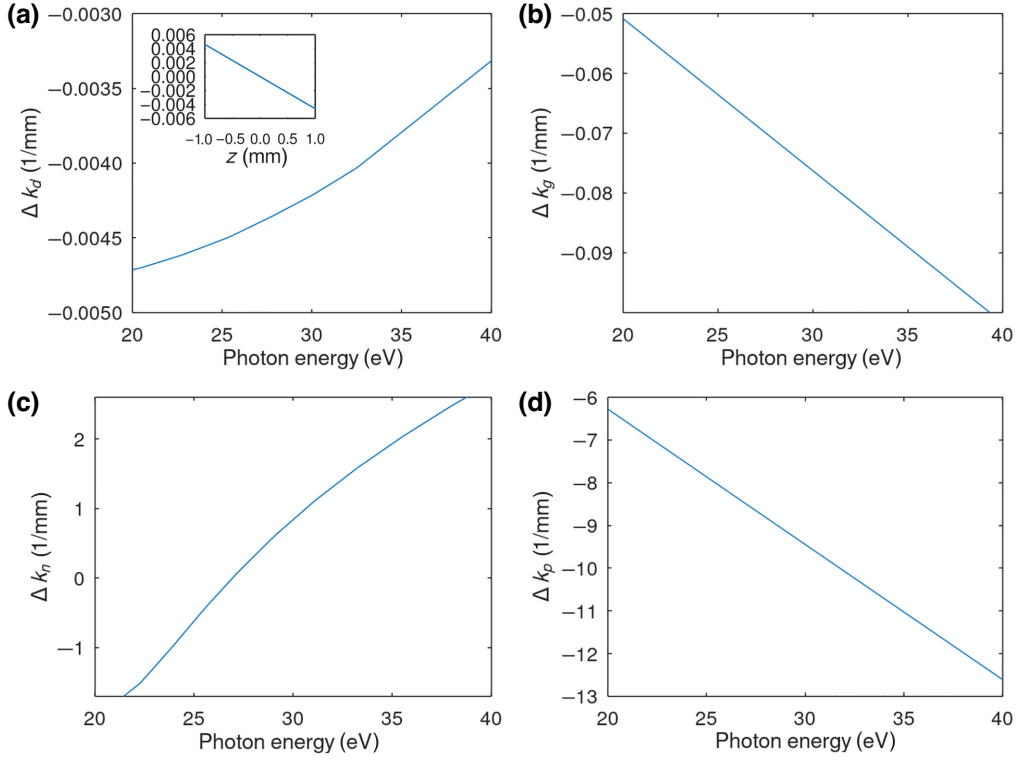


FIG. 7. The four phase mismatch terms of Eq. (C3) in the order of lowest to highest contribution to total phase mismatch for the studied scenario. (a) The dipole phase related phase mismatch term Δk_d for long trajectories as a function of photon energy at 1-mm distance from focus. The inset shows the distance dependence of this factor for 30 eV. (b) The geometric phase related phase mismatch term Δk_g as a function of photon energy. The plot clearly shows the linear increase with photon energy (harmonic order; see text for details). (c) The neutral dispersion related phase mismatch term Δk_n as a function of photon energy for the highest atom number density relevant for the studied case, 2×10^{18} $1/\text{cm}^3$. (d) The plasma dispersion related phase mismatch term Δk_p as a function of photon energy for 2×10^{18} $1/\text{cm}^3$ number density and 5% ionization rate.

with the textbook expression of on-axis intensity variation $I(z)$ of Gaussian beams, giving

$$\frac{\partial I(z)}{\partial z} = -I_0 \frac{2L_R^2 z}{(L_R^2 + z^2)^2}. \quad (\text{C5})$$

We applied the peak intensity of $I_0 = 3.3 \times 10^{14}$ W/cm^2 and Rayleigh length of $L_R = 260$ mm, both values originating from the macroscopic simulations. The dipole phase coefficient α was extracted from Ref. [72], having a typical value of approximately 40×10^{-14} cm^2/W for long trajectories, while an order of magnitude lower for short trajectories [78], the latter of which usually dominate the HHG signal. The plot in Fig. 7(a) shows the result for long trajectories at a 1-mm distance from focus [with its value being zero in focus changing linearly with the distance from focus within the relevant distance range; see inset of Fig. 7(a)]. Here Δk_d has only a weak dependence on harmonic order q (or photon energy) through the variation of $\alpha = \alpha(q)$ [50,72].

Because of the small interaction distance (< 1 mm) compared with the Rayleigh length of the focused beam ($L_R =$

260 mm), the geometric phase induced mismatch term is constant over the interaction length [50], showing a linear dependence with harmonic order q according to [see Eq. (5) of Ref. [50]]

$$\Delta k_q = -\frac{q}{L_R}; \quad (\text{C6})$$

as can be seen in Fig. 7(b).

Neutral dispersion also causes phase mismatch, Δk_n , which depends on the refractive index of the generation medium at the wavelength of the generating field and the generated XUV according to Eq. (7) of Ref. [50], that is,

$$\Delta k_n = q \frac{\omega_1}{c} (n_1 - n_q), \quad (\text{C7})$$

where $\omega_1 = 2\pi c/\lambda$ is the central angular frequency of the laser field and c is the speed of light in vacuum. The refractive index n_1 for the central wavelength of $\lambda = 830$ nm was obtained from Ref. [79]. In the case of XUV photon energies, the refractive index n_q was calculated based on expressions in Ref. [66] using atomic scattering form

factors from the National Institute of Standards and Technology (NIST) [80]. In case of both refractive indices, n_1 and n_q , it stands that $(n - 1) \sim \rho$, that is, their difference from 1 is proportional to the number density. The resulting phase mismatch is plotted in Fig. 7(c) as a function of photon energy for the highest number density involved in this study, $\rho = 2 \times 10^{18} \text{ 1/cm}^3$ (see the density values at $z = 400 \text{ }\mu\text{m}$ distance from the nozzle orifice, where the laser beam propagates through in Fig. 2 or Fig. 3). The ionization—and the plasma generated—is a key factor tuning phase matching through the term Δk_p . This phase mismatch term was calculated using Eq. (8) of Ref. [50], which reads as

$$\Delta k_p = q \frac{\omega_1}{c} (n_1^e - n_q^e), \quad (\text{C8})$$

defined by the plasma refractive index $n_q^e = \sqrt{1 - N_e/N_c}$, where $N_e = \Gamma\rho$ is the number density of free electrons (Γ being the ionization ratio and ρ the atom number density). The photon energy dependence of plasma refractive index appears through the critical density $N_c = \varepsilon_0 m \omega^2 / e^2$ (with vacuum permittivity ε_0 , electron mass m , electron charge e , and angular frequency ω). The resulting values of Δk_p are plotted in Fig. 7(d) as a function of photon energy for $\rho = 2 \times 10^{18} \text{ 1/cm}^3$ density and an ionization ratio of $\Gamma = 5\%$ (this choice of ionization ratio will be explained later). This phase mismatch term is proportional both to density and ionization ratio [26], that is, $\Delta k_p \sim \rho\Gamma$ (see explicit expressions for both Δk_n and Δk_p in Ref. [26]).

The most important observations related to the phase mismatch terms in Fig. 7 are the following. As is known, dipole and geometric phase related terms are independent of the number density of atoms, while the other two are proportional to it [26]. Also, the two density-independent terms are orders of magnitude lower than the density-dependent terms in our current conditions, reaching comparable values only when the pressure in the medium is $<5\%$ of the peak value (cf. phase mismatch values in Fig. 7, which will also be confirmed later). This means that the total phase mismatch Δk of Eq. (C3) will be proportional to the density ρ for a pressure range where there is relevant harmonic flux, and according to Eq. (C2) the coherence length will be inversely proportional to the density: $L_{\text{coh}} \sim 1/\rho$. It is worth noting additionally that, for the ionization rates involved, the plasma related term Δk_p is an order of magnitude higher even compared with the Δk_n term, meaning that ionization is dominating the phase matching conditions in these experiments.

Although certain phase mismatch term(s) dominate(s) the macroscopic flux, we calculated the coherence length taking into account all Δk terms in Eq. (C3), and plotted it in Fig. 8(a) as a function of number density for different photon energies. The shape of all curves in Fig. 8(a) confirm that the neutral and plasma dispersion (especially

the second) dominate the coherence length, as they show $L_{\text{coh}} \sim 1/\rho$ dependence.

As is known, the absorption length L_{abs} only depends on the medium through the material-specific photoionization cross section σ and the medium density ρ according to [25]

$$L_{\text{abs}} = 1/\sigma\rho. \quad (\text{C9})$$

Photoionization cross sections in the XUV can be obtained from measured atomic scattering form factors (for example, from the NIST database [80]) similarly as described in Ref. [26], giving the photon energy dependence of σ . Corresponding absorption lengths as a function of atom number density (in the density range relevant for the cases in the main text) for different photon energies are plotted in Fig. 8(b), showing the expected variations: the absorption length decreases with the increase of both number density and photon energy.

The fact that both L_{coh} and L_{abs} are inversely proportional to the number density is of key importance when analyzing the flux using the model of Constant *et al.* [25] in the current scenario. Since the ratio of these two parameters, $L_{\text{coh}}/L_{\text{abs}}$, is independent of pressure, the number of variables in the Constant model can be decreased to two from three. This practically means that the pressure dependence of XUV flux at a certain photon energy can be studied by analyzing the shape of one single curve in the plot of Fig. 6. The photon energy to which each curve corresponds to (in the studied experimental case) is indicated in parentheses in the legend of Fig. 6. Also, since the absorption length is inversely proportional to the medium pressure, changing the pressure simply means a different value of medium length $L = L_{\text{med}}/2L_{\text{abs}}$ on the horizontal axis of Fig. 6. Since a pressure increase means a decrease of absorption length, for a fixed medium length (like in our case), pressure increase means a higher value of L . Since the medium length in our case is in the range of $L_{\text{med}} = 400 \text{ }\mu\text{m}$, the value of L has an upper limit of $L < 3$ based on absorption lengths plotted in Fig. 8(b). In Fig. 6 the rectangles on each curve indicate the value L that corresponds to $\rho = 2 \times 10^{18} \text{ 1/cm}^3$. Lower pressures mean smaller values of L .

Figure 9(a) shows the spatiotemporal profile of the generated attosecond burst in the detection plane calculated with the macroscopic model. It can be seen that there are two half-cycles in the time window that reach the detector and are dominant. These are located between -0.75 and -0.25 optical cycles (o.c.) in this moving time window fixed to the middle of the pulse [see green rectangle in Fig. 9(a)]. In Fig. 9(b) the on-axis temporal evolution of the laser electric field and corresponding ionization ratios are plotted in the same time window for the two ends of the generation medium. As can be seen, the laser electric field is minimally reshaped during propagation through

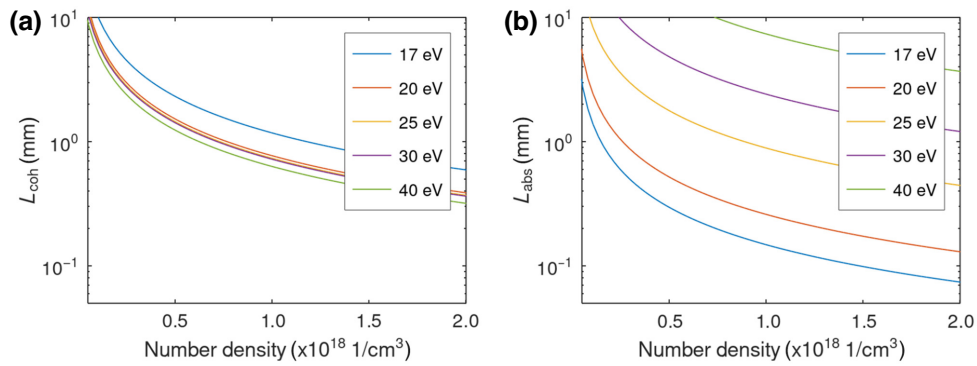


FIG. 8. (a) Coherence length L_{coh} as a function of Ar atom number density for different photon energies calculated using Eq. (C2) and the phase mismatch values plotted in Fig. 7. (b) Absorption length L_{abs} in Ar as a function of atom number density for different photon energies in the XUV calculated using Eq. (C9).

the medium, and corresponding ionization rates also differ only by a few percent. As a result, the assumption of the simple model that the single-atom response A is constant throughout the generation volume holds for this experimental case. The most important information available from Fig. 9(b) is that the time window from which the dominant part of the high-harmonic field originates is the same in the whole generation medium, and in this time window the ionization ratio is in the range of approximately 5–10%. This is the reason for the ionization rates applied when calculating the phase mismatch term Δk_p in Fig. 7(d). This few percent ionization level matches approximately (in our case the ratios being slightly higher) the well-known property that best phase matching is possible in case of low ionization levels considering traditional phase matching scenarios [50]. It also explains why those

certain attosecond bursts are dominant: in half-cycles that are before -0.75 o.c. the signal is lower because of a lower number of photons (see the rate of ionization level change that is related to the number of photons emitted). Additionally, in half-cycles after -0.25 o.c., a large number of photons are generated (bigger changes in ionization level in Fig. 9), but due to high ionization levels the coherence lengths are shorter, phase matching is worse compared with the $[-0.75, -0.25]$ o.c. temporal window.

The main conclusions of this analysis are plotted in Fig. 10. Figure 10(a) confirms the assumption that, for the relevant pressure range, the value of R_0 is independent of pressure, and a single curve of Fig. 6 describes the flux for a certain harmonic. In Fig. 10(b) the harmonic flux as a function of Ar atom number density is plotted for different photon energies. This plot is basically rescaling the

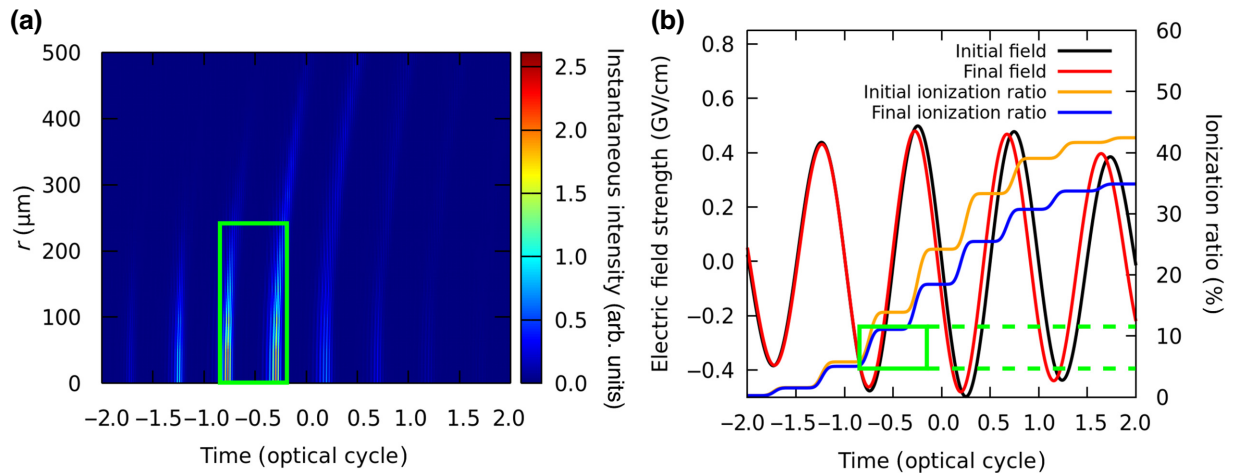


FIG. 9. (a) The spatiotemporal distribution of the high-harmonic field in the detector plane. The time axis is in units of optical cycles corresponding to the central wavelength 830 nm of the laser field, that is 2.77 fs. The green box indicates the two dominant attosecond bursts. (b) The on-axis temporal evolution of the laser electric field at the beginning (“initial”) and end of the generation medium (“final”) and the corresponding time evolution of ionization rates. The green box indicates the same time window as in (a), the dashed line shows corresponding ionization rates.

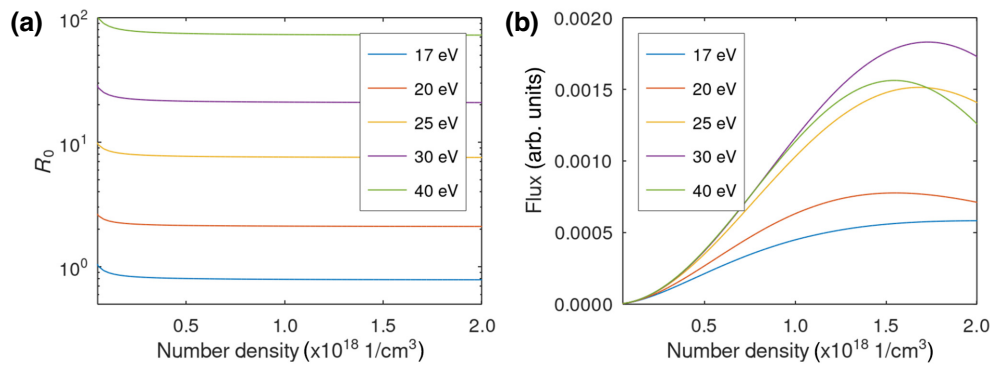


FIG. 10. (a) The R_0 parameter defining the ratio of coherence and absorption lengths as a function of atom density for different photon energies, obtained from values plotted in Fig. 8. (b) The harmonic flux as a function of atom number density calculated using the simple model of Constant *et al.* [25,26] [see Eq. (C1)]. The R_1 values are from (a), absorption lengths are from Fig. 8(b), and the medium length is $L_{\text{med}} = 400 \mu\text{m}$.

curves of Fig. 6 between $L = 0$ and L indicated by the rectangle on each curve in Fig. 6 according to how L_{abs} changes with ρ for the specific photon energy. Actually, to obtain these curves the coherence and absorption length values were calculated similarly as for Fig. 8, and used in Eq. (C1), applying a medium length of $L_{\text{med}} = 400 \mu\text{m}$. The curves of Fig. 10(b) show proportionality of harmonic flux with medium pressure, with slight saturation towards the higher densities. The plotted flux also shows what was observed in the macroscopic simulations and experiments: the phase matching conditions are the best—and the flux is highest—for photon energies between 25 and 40 eV.

Lifschitz, and J. Faure, Relativistic electron beams driven by kHz single-cycle light pulses, *Nat. Photonics* **11**, 293 (2017).

- [1] S. Toth, T. Stanislauskas, I. Balciunas, R. Budriunas, J. Adamonis, R. Danilevicius, K. Viskontas, D. Lengvinas, G. Veitas, D. Gadonas, A. Varanavičius, J. Csontos, T. Somoskoi, L. Toth, A. Borzsonyi, and K. Osvay, SYLOS lasers—the frontier of few-cycle, multi-TW, kHz lasers for ultrafast applications at extreme light infrastructure attosecond light pulse source, *J. Phys. Photonics* **2**, 045003 (2020).
- [2] M. Ouillé, A. Vernier, F. Böhle, M. Bocoum, A. Jullien, M. Lozano, J.-P. Rousseau, Z. Cheng, D. Gustas, A. Blumenstein, P. Simon, S. Haessler, J. Faure, T. Nagy, and R. Lopez-Martens, Relativistic-intensity near-single-cycle light waveforms at kHz repetition rate, *Light: Sci. Appl.* **9**, 47 (2020).
- [3] M. Stanfield, N. F. Beier, S. Hakimi, H. Allison, D. Farinella, A. E. Hussein, T. Tajima, and F. Dollar, Millijoule few-cycle pulses from staged compression for strong and high field science, *Opt. Express* **29**, 9123 (2021).
- [4] F. J. Furch, T. Witting, M. Osolodkov, F. Schell, C. P. Schulz, and M. J. J. Vrakking, High power, high repetition rate laser-based sources for attosecond science, *J. Phys.: Photonics* **4**, 032001 (2022).
- [5] D. Guénot, D. Gustas, A. Vernier, B. Beaupaire, F. Böhle, M. Bocoum, M. Lozano, A. Jullien, R. Lopez-Martens, A. Lifschitz, and J. Faure, Relativistic electron beams driven by kHz single-cycle light pulses, *Nat. Photonics* **11**, 293 (2017).
- [6] J. Huijts, L. Rovige, I. A. Andriyash, A. Vernier, M. Ouillé, J. Kaur, Z. Cheng, R. Lopez-Martens, and J. Faure, Waveform control of relativistic electron dynamics in laser-plasma acceleration, *Phys. Rev. X* **12**, 011036 (2022).
- [7] S. Mikaelsson, J. Vogelsang, C. Guo, I. Sytceвич, A.-L. Viotti, F. Langer, Y.-C. Cheng, S. Nandi, W. Jin, A. Olofsson, R. Weissenbilder, J. Mauritsson, A. L’Huillier, M. Gisselbrecht, and C. L. Arnold, A high-repetition rate attosecond light source for time-resolved coincidence spectroscopy, *Nanophotonics* **10**, 117 (2020).
- [8] T. Witting, M. Osolodkov, F. Schell, F. Morales, S. Patchkovskii, P. Šušnjar, F. H. M. Cavalcante, C. S. Menoni, C. P. Schulz, F. J. Furch, and M. J. J. Vrakking, Generation and characterization of isolated attosecond pulses at 100 kHz repetition rate, *Optica* **9**, 145 (2022).
- [9] P. Ye, L. G. Oldal, T. Csizmadia, Z. Filus, T. Grósz, P. Jójárt, I. Seres, Z. Bengery, B. Gilicze, S. Kahaly, K. Varjú, and B. Major, High-flux 100 kHz attosecond pulse source driven by a high-average power annular laser beam, *Ultrafast Sci.* **2022**, 9823783 (2022).
- [10] T. Csizmadia, Z. Filus, T. Grósz, P. Ye, L. G. Oldal, M. D. Marco, P. Jójárt, I. Seres, Z. Bengery, B. Gilicze, M. Lucchini, M. Nisoli, F. Frassetto, F. Samparisi, L. Poletto, K. Varjú, S. Kahaly, and B. Major, Spectrally tunable ultrashort monochromatized extreme ultraviolet pulses at 100 kHz, *APL Photonics* **8**, 056105 (2023).
- [11] F. Sylla, M. Veltcheva, S. Kahaly, A. Flacco, and V. Malka, Development and characterization of very dense submillimetric gas jets for laser-plasma interaction, *Rev. Sci. Instrum.* **83**, 033507 (2012).
- [12] D. Irímia, D. Dobrikov, R. Kortekaas, H. Voet, D. A. van den Ende, W. A. Groen, and M. H. M. Janssen, A short pulse (7 μs FWHM) and high repetition rate (dc-5 kHz) cantilever piezovalve for pulsed atomic and molecular beams, *Rev. Sci. Instrum.* **80**, 113303 (2009).
- [13] D. Irímia, R. Kortekaas, and M. H. M. Janssen, In situ characterization of a cold and short pulsed molecular beam by femtosecond ion imaging, *Phys. Chem. Chem. Phys.* **11**, 3958 (2009).

- [14] U. Even, Pulsed supersonic beams from high pressure source: Simulation results and experimental measurements, *Adv. Chem.* **2014**, 1 (2014).
- [15] C. Meng and M. H. M. Janssen, Measurement of the density profile of pure and seeded molecular beams by femtosecond ion imaging, *Rev. Sci. Instrum.* **86**, 023110 (2015).
- [16] T. Pak, M. Rezaei-Pandari, S. B. Kim, G. Lee, D. H. Wi, C. I. Hojbota, M. Mirzaie, H. Kim, J. H. Sung, S. K. Lee, C. Kang, and K.-Y. Kim, Multi-millijoule terahertz emission from laser-wakefield-accelerated electrons, *Light: Sci. Appl.* **12**, 37 (2023).
- [17] X.-L. Zhu, S.-M. Weng, M. Chen, Z.-M. Sheng, and J. Zhang, Efficient generation of relativistic near-single-cycle mid-infrared pulses in plasmas, *Light: Sci. Appl.* **9**, 46 (2020).
- [18] Z. Nie, C.-H. Pai, J. Zhang, X. Ning, J. Hua, Y. He, Y. Wu, Q. Su, S. Liu, Y. Ma, Z. Cheng, W. Lu, H.-H. Chu, J. Wang, C. Zhang, W. B. Mori, and C. Joshi, Photon deceleration in plasma wakes generates single-cycle relativistic tunable infrared pulses, *Nat. Commun.* **11**, 2787 (2020).
- [19] X. Ren, V. Makhija, A.-T. Le, J. Troß, S. Mondal, C. Jin, V. Kumarappan, and C. Trallero-Herrero, Measuring the angle-dependent photoionization cross section of nitrogen using high-harmonic generation, *Phys. Rev. A* **88**, 043421 (2013).
- [20] J. Troß, X. Ren, V. Makhija, S. Mondal, V. Kumarappan, and C. A. Trallero-Herrero, N₂ HOMO-1 orbital cross section revealed through high-order-harmonic generation, *Phys. Rev. A* **95**, 033419 (2017).
- [21] V. Leshchenko, S. J. Hageman, C. Cariker, G. Smith, A. Camper, B. K. Talbert, P. Agostini, L. Argenti, and L. F. DiMauro, Kramers–kronig relation in attosecond transient absorption spectroscopy, *Optica* **10**, 142 (2023).
- [22] M. Ferray, A. L’Huillier, X. F. Li, L. A. Lompre, G. Mainfray, and C. Manus, Multiple-harmonic conversion of 1064 nm radiation in rare gases, *J. Phys. B: At., Mol. Opt. Phys.* **21**, L31 (1988).
- [23] A. Nayak, *et al.*, Saddle point approaches in strong field physics and generation of attosecond pulses, *Phys. Rep.* **833**, 1 (2019).
- [24] K. Amini, *et al.*, Symphony on strong field approximation, *Rep. Progr. Phys.* **82**, 116001 (2019).
- [25] E. Constant, D. Garzella, P. Breger, E. Mével, C. Dorrer, C. L. Blanc, F. Salin, and P. Agostini, Optimizing high harmonic generation in absorbing gases: Model and experiment, *Phys. Rev. Lett.* **82**, 1668 (1999).
- [26] B. Major and K. Varjú, Extended model for optimizing high-order harmonic generation in absorbing gases, *J. Phys. B: At., Mol. Opt. Phys.* **54**, 224002 (2021).
- [27] S. Kühn, *et al.*, The ELI-ALPS facility: The next generation of attosecond sources, *J. Phys. B: At., Mol. Opt. Phys.* **50**, 132002 (2017).
- [28] D. Charalambidis, V. Chikán, E. Cormier, P. Dombi, J. A. Fülöp, C. Janáky, S. Kahaly, M. Kalashnikov, C. Kamperidis, S. Kühn, F. Lepine, A. L’Huillier, R. Lopez-Martens, S. Mondal, K. Osvay, L. Óvári, P. Rudawski, G. Sansone, P. Tzallas, Z. Várallyay, and K. Varjú, in *Progress in Ultrafast Intense Laser Science XIII, Springer Series in Chemical Physics*, edited by K. Yamanouch, W. T., Hill III, and G. G. Paulus (Springer, Cham, 2017), p. 181.
- [29] A. Nayak, I. Orfanos, I. Makos, M. Dumergue, S. Kühn, E. Skantzakis, B. Bodi, K. Varju, C. Kalpouzos, H. I. B. Banks, A. Emmanouilidou, D. Charalambidis, and P. Tzallas, Multiple ionization of argon via multi-XUV-photon absorption induced by 20-GW high-order harmonic laser pulses, *Phys. Rev. A* **98**, 023426 (2018).
- [30] B. Manschwetus, L. Rading, F. Campi, S. Maclot, H. Coudert-Alteirac, J. Lahl, H. Wikmark, P. Rudawski, C. M. Heyl, B. Farkas, T. Mohamed, A. L’Huillier, and P. Johnsson, Two-photon double ionization of neon using an intense attosecond pulse train, *Phys. Rev. A* **93**, 061402 (2016).
- [31] I. Orfanos, I. Makos, I. Lontos, E. Skantzakis, B. Major, A. Nayak, M. Dumergue, S. Kühn, S. Kahaly, K. Varju, G. Sansone, B. Witzel, C. Kalpouzos, L. A. A. Nikolopoulos, P. Tzallas, and D. Charalambidis, Non-linear processes in the extreme ultraviolet, *J. Phys.: Photonics* **2**, 042003 (2020).
- [32] I. Orfanos, E. Skantzakis, A. Nayak, M. Dumergue, S. Kühn, G. Sansone, M. F. Kling, H. Schröder, B. Bergues, J. Csontos, S. Toth, Á. Börzönyi, S. Kahaly, K. Varjú, A. Forembki, L. A. A. Nikolopoulos, P. Tzallas, and D. Charalambidis, Two-XUV-photon double ionization of neon, *Phys. Rev. A* **106**, 043117 (2022).
- [33] B. Major, O. Ghafur, K. Kovács, K. Varjú, V. Tosa, M. J. J. Vrakking, and B. Schütte, Compact intense extreme-ultraviolet source, *Optica* **8**, 960 (2021).
- [34] A. Comby, S. Beaulieu, E. Constant, D. Descamps, S. Petit, and Y. Mairesse, Absolute gas density profiling in high-order harmonic generation, *Opt. Express* **26**, 6001 (2018).
- [35] C. Altucci, C. Beneduce, R. Bruzzese, C. de Lisio, G. S. Sorrentino, T. Starczewski, and F. Vigilante, Characterization of pulsed gas sources for intense laser field—atom interaction experiments, *J. Phys. D: Appl. Phys.* **29**, 68 (1996).
- [36] F. Brandi and F. Giammanco, Temporal and spatial characterization of a pulsed gas jet by a compact high-speed high-sensitivity second-harmonic interferometer, *Opt. Express* **19**, 25479 (2011).
- [37] H. Xu, G. Chen, D. N. Patel, Y. Cao, L. Ren, H. Xu, H. Shao, J. He, and D. E. Kim, Gas density distribution in a clustered-gas jet produced from a supersonic slit nozzle under high backing pressure, *AIP Adv.* **11**, 075313 (2021).
- [38] B. Hagmeister, D. Hemmers, and G. Pretzler, Characterization of a pulsed, supersonic gas jet by absorption of high-order harmonics in the extreme ultraviolet spectral range, *Appl. Phys. B* **128**, 172 (2022).
- [39] O. F. Hagen, Nucleation and growth of clusters in expanding nozzle flows, *Surf. Sci.* **106**, 101 (1981).
- [40] O. F. Hagen, Cluster ion sources (invited), *Rev. Sci. Instrum.* **63**, 2374 (1992).
- [41] B. R. Lee, P. K. Singh, Y. J. Rhee, and C. H. Nam, Spatiotemporal characteristics of high-density gas jet and absolute determination of size and density of gas clusters, *Sci. Rep.* **10**, 12973 (2020).
- [42] M. Takeda, H. Ina, and S. Kobayashi, Fourier-transform method of fringe-pattern analysis for computer-based topography and interferometry, *J. Opt. Soc. Am.* **72**, 156 (1982).

- [43] N. H. Abel, Auflösung einer mechanischen Aufgabe., *J. Angew. Math.* **1826**, 153 (1826).
- [44] V. Dribinski, A. Ossadtchi, V. A. Mandelshtam, and H. Reisler, Reconstruction of abel-transformable images: The Gaussian basis-set expansion abel transform method, *Rev. Sci. Instrum.* **73**, 2634 (2002).
- [45] D. D. Hickstein, S. T. Gibson, R. Yurchak, D. D. Das, and M. Ryazanov, A direct comparison of high-speed methods for the numerical Abel transform, *Rev. Sci. Instrum.* **90**, 1 (2019).
- [46] R. Budriūnas, T. Stanislauskas, J. Adamonis, A. Aleknavičius, G. Veitas, D. Gadonas, S. Balickas, A. Michailovas, and A. Varanavičius, 53 W average power CEP-stabilized OPCPA system delivering 55 TW few cycle pulses at 1 kHz repetition rate, *Opt. Express* **25**, 5797 (2017).
- [47] C. E. Repetto, A. Roatta, and R. J. Welti, Forced vibrations of a cantilever beam, *Eur. J. Phys.* **33**, 1187 (2012).
- [48] L. Drescher, O. Kornilov, T. Witting, G. Reitsma, N. Monserud, A. Rouzée, J. Mikosch, M. J. J. Vrakking, and B. Schütte, Extreme-ultraviolet refractive optics, *Nature* **564**, 91 (2018).
- [49] M. Hoflund, J. Peschel, M. Plach, H. Dacasa, K. Veyrinas, E. Constant, P. Smorenburg, H. Wikmark, S. Maclot, C. Guo, C. Arnold, A. L’Huillier, and P. Eng-Johnsson, Focusing properties of high-order harmonics, *Ultrafast Sci.* **2021**, 9797453 (2021).
- [50] C. M. Heyl, C. L. Arnold, A. Couairon, and A. L’Huillier, Introduction to macroscopic power scaling principles for high-order harmonic generation, *J. Phys. B: At., Mol. Opt. Phys.* **50**, 013001 (2016).
- [51] Y. Tao, S. J. Goh, H. M. J. Bastiaens, P. J. M. van der Slot, S. G. Biedron, S. V. Milton, and K. J. Boller, Temporal model for quasi-phase matching in high-order harmonic generation, *Opt. Express* **25**, 3621 (2017).
- [52] Z. Fu, Y. Chen, S. Peng, B. Zhu, B. Li, R. Martín-Hernández, G. Fan, Y. Wang, C. Hernández-García, C. Jin, M. Murnane, H. Kapteyn, and Z. Tao, Extension of the bright high-harmonic photon energy range via nonadiabatic critical phase matching, *Sci. Adv.* **8**, eadd7482 (2022).
- [53] V. Tosa, K. T. Kim, and C. H. Nam, Macroscopic generation of attosecond-pulse trains in strongly ionized media, *Phys. Rev. A* **79**, 043828 (2009).
- [54] E. Priori, G. Cerullo, M. Nisoli, S. Stagira, S. De Silvestri, P. Villoresi, L. Poletto, P. Ceccherini, C. Altucci, R. Bruzzese, and C. de Lisio, Nonadiabatic three-dimensional model of high-order harmonic generation in the few-optical-cycle regime, *Phys. Rev. A* **61**, 063801 (2000).
- [55] B. Major, K. Kovács, V. Tosa, P. Rudawski, A. L’Huillier, and K. Varjú, Effect of plasma-core-induced self-guiding on phase matching of high-order harmonic generation in gases, *J. Opt. Soc. Am. B* **36**, 1594 (2019).
- [56] V. Tosa, K. Kovács, B. Major, E. Balogh, and K. Varjú, Propagation effects in highly ionised gas media, *Quantum Electron.* **46**, 321 (2016).
- [57] Z. Chang, in *Fundamentals of Attosecond Optics* (CRC Press, Boca Raton, 2011), p. 547.
- [58] M. Geissler, G. Tempea, A. Scrinzi, M. Schnürer, F. Krausz, and T. Brabec, Light propagation in field-ionizing media: Extreme nonlinear optics, *Phys. Rev. Lett.* **83**, 2930 (1999).
- [59] M. Ibnchaikh and A. Belafhal, The ABCD-Hankel transformation in two-dimensional frequency-domain with polar coordinates, *Phys. Chem. News* **2**, 29 (2001).
- [60] B. Major, Z. L. Horváth, and K. Varjú, Spatial characterization of light beams analyzed by cylindrical-grating slit-less spectrometers, *Appl. Opt.* **57**, 738 (2018).
- [61] M. Lewenstein, P. Balcou, M. Ivanov, A. L’Huillier, and P. B. Corkum, Theory of high-harmonic generation by low-frequency laser fields, *Phys. Rev. A* **49**, 2117 (1994).
- [62] A.-T. Le, R. R. Lucchese, S. Tonzani, T. Morishita, and C. D. Lin, Quantitative rescattering theory for high-order harmonic generation from molecules, *Phys. Rev. A* **80**, 013401 (2009).
- [63] V. P. Majety and A. Scrinzi, Static field ionization rates for multi-electron atoms and small molecules, *J. Phys. B: At., Mol. Opt. Phys.* **48**, 245603 (2015).
- [64] M. V. Ammosov, N. B. Delone, and V. P. Krainov, Tunnel ionization of complex atoms and of atomic ions in an alternating electromagnetic field, *Sov. Phys. JETP* **64**, 1191 (1987).
- [65] M. B. Gaarde, J. L. Tate, and K. J. Schafer, Macroscopic aspects of attosecond pulse generation, *J. Phys. B: At., Mol. Opt. Phys.* **41**, 132001 (2008).
- [66] B. Henke, E. Gullikson, and J. Davis, X-ray interactions: Photoabsorption, scattering, transmission, and reflection at $e = 50\text{--}30\,000$ eV, $z = 1\text{--}92$, *At., Data Nucl. Data Tables* **54**, 181 (1993).
- [67] J. Schötz, B. Förg, W. Schweinberger, I. Lontos, H. A. Masood, A. M. Kamal, C. Jakubeit, N. G. Kling, T. Paasch-Colberg, S. Biswas, M. Högnér, I. Pupeza, M. Alharbi, A. M. Azzeer, and M. F. Kling, Phase-matching for generation of isolated attosecond XUV and soft-X-ray pulses with few-cycle drivers, *Phys. Rev. X* **10**, 041011 (2020).
- [68] B. Schütte, P. Weber, K. Kovács, E. Balogh, B. Major, V. Tosa, S. Han, M. J. J. Vrakking, K. Varjú, and A. Rouzée, Bright attosecond soft X-ray pulse trains by transient phase-matching in two-color high-order harmonic generation, *Opt. Express* **23**, 33947 (2015).
- [69] R. Weissenbilder, S. Carlström, L. Rego, C. Guo, C. M. Heyl, P. Smorenburg, E. Constant, C. L. Arnold, and A. L’Huillier, How to optimize high-order harmonic generation in gases, *Nat. Rev. Phys.* **4**, 713 (2022).
- [70] E. Appi, R. Weissenbilder, B. Nagyillés, Z. Diveki, J. Peschel, B. Farkas, M. Plach, F. Vismarra, V. Poulain, N. Weber, C. L. Arnold, K. Varjú, S. Kahaly, P. Eng-Johnsson, and A. L’Huillier, and Two phase-matching regimes in high-order harmonic generation, *Opt. Express* **31**, 31687 (2023).
- [71] S. Chatziathanasiou, I. Lontos, E. Skantzakis, S. Kahaly, M. U. Kahaly, N. Tsatrafyllis, O. Faucher, B. Witzel, N. Papadakis, D. Charalambidis, and P. Tzallas, Quantum path interferences in high-order harmonic generation from aligned diatomic molecules, *Phys. Rev. A* **100**, 061404 (2019).
- [72] T. Csizmadia, L. G. Oldal, P. Ye, S. Majorosi, P. Tzallas, G. Sansone, V. Tosa, K. Varjú, B. Major, and S. Kahaly, Detailed study of quantum path interferences in high harmonic generation driven by chirped laser pulses, *New J. Phys.* **23**, 123012 (2021).

- [73] A. Lifschitz, F. Sylla, S. Kahaly, A. Flacco, M. Veltcheva, G. Sanchez-Arriaga, E. Lefebvre, and V. Malka, Ion acceleration in underdense plasmas by ultra-short laser pulses, *New J. Phys.* **16**, 033031 (2014).
- [74] S. Kahaly, F. Sylla, A. Lifschitz, A. Flacco, M. Veltcheva, and V. Malka, Detailed experimental study of ion acceleration by interaction of an ultra-short intense laser with an underdense plasma, *Sci. Rep.* **6**, 31647 (2016).
- [75] H. Wikmark, C. Guo, J. Vogelsang, P. W. Smorenburg, H. Coudert-Alteirac, J. Lahl, J. Peschel, P. Rudawski, H. Dacasa, S. Carlström, S. Maclot, M. B. Gaarde, P. Johnsson, C. L. Arnold, A. L'Huillier, and Spatiotemporal coupling of attosecond pulses, Spatiotemporal coupling of attosecond pulses, *Proc. Natl. Acad. Sci.* **116**, 4779 (2019).
- [76] A. Dubrouil, O. Hort, F. Catoire, D. Descamps, S. Petit, E. Mével, V. V. Strelkov, and E. Constant, Spatio-spectral structures in high-order harmonic beams generated with terawatt 10-fs pulses, *Nat. Commun.* **5**, 4697 (2014).
- [77] <https://www.amsterdampiezovalve.com/specifications>.
- [78] S. Carlström, J. Preclíková, E. Lorek, E. W. Larsen, C. M. Heyl, D. Palecek, D. Zigmantas, K. J. Schafer, M. B. Gaarde, and J. Mauritsson, Spatially and spectrally resolved quantum path interference with chirped driving pulses, *New J. Phys.* **18**, 123032 (2016).
- [79] <https://refractiveindex.info/?shelf=main&book=Ar&page=Bideau-Mehu>.
- [80] https://henke.lbl.gov/optical_constants/sf/ar.nff.